

# Twisted Trilayer Graphene: A Precisely Tunable Platform for Correlated Electrons

Ziyan Zhu<sup>1</sup>, Stephen Carr,<sup>1</sup> Daniel Massatt,<sup>2</sup> Mitchell Luskin<sup>3</sup>, and Efthimios Kaxiras<sup>1,4</sup>

<sup>1</sup>Department of Physics, Harvard University, Cambridge, Massachusetts 02138, USA

<sup>2</sup>Department of Statistics, The University of Chicago, Chicago, Illinois 60637, USA

<sup>3</sup>School of Mathematics, University of Minnesota—Twin Cities, Minneapolis, Minnesota 55455, USA

<sup>4</sup>John A. Paulson School of Engineering and Applied Sciences, Harvard University, Cambridge, Massachusetts 02138, USA



(Received 30 May 2020; accepted 29 July 2020; published 11 September 2020)

We introduce twisted trilayer graphene (tTLG) with two independent twist angles as an ideal system for the precise tuning of the electronic interlayer coupling to maximize the effect of correlated behaviors. As established by experiment and theory in the related twisted bilayer graphene system, van Hove singularities (VHS) in the density of states can be used as a proxy of the tendency for correlated behaviors. To explore the evolution of VHS in the twist-angle phase space of tTLG, we present a general low-energy electronic structure model for any pair of twist angles. We show that the basis of the model has infinite dimensions even at a finite energy cutoff and that no Brillouin zone exists even in the continuum limit. Using this model, we demonstrate that the tTLG system exhibits a wide range of magic angles at which VHS merge and that the density of states has a sharp peak at the charge-neutrality point through two distinct mechanisms: the incommensurate perturbation of twisted bilayer graphene’s flatbands or the equal hybridization between two bilayer moiré superlattices.

DOI: 10.1103/PhysRevLett.125.116404

**Introduction.**—Electronic properties in stacked graphene layers can be tuned by a small twist angle that modifies the interlayer interaction strength, an effect referred to as “twistronics” [1]. As the twist angle approaches a critical “magic angle” ( $\sim 1.05^\circ$  in twisted bilayer graphene), the two van Hove singularities (VHS) in the density of states (DOS) of each monolayer merge, resulting in a sharp peak associated with flatbands, leading to the emergence of strongly correlated electronic phases [2]. The small twist angle gives rise to large-scale repeating patterns known as moiré patterns. Unconventional correlated states have now been observed in many van der Waals (vdW) heterostructures with one twist angle, e.g., twisted bilayer graphene (tBLG) and twisted double bilayer graphene [3–15]. In these systems, electrons responsible for the correlation effects localize at the moiré scale [16–18].

The addition of a third layer introduces a new degree of freedom, the second twist angle, allowing for the further tuning of electron correlations. In twisted trilayer graphene (tTLG) with two consecutive twist angles,  $\theta_{12}$  and  $\theta_{23}$ , the beating of two bilayer moiré patterns leads to higher-order patterns (moiré of moiré). The length scale of these is orders of magnitude larger than the bilayer moiré [Fig. 1(a)] [19–21]. Unlike in tBLG where only the lowest-order moiré pattern dominates in the continuum limit, the dominant harmonic is twist-angle dependent in tTLG. For a given moiré of moiré harmonic labeled by  $(m, n)$ , the primitive reciprocal lattice vectors are given as the column vectors of  $G_{mn}^H = mG_{12} - nG_{23}$ , where the matrix  $G_{ij}$  spans the bilayer moiré reciprocal space between layers

$i$  ( $L_i$ ) and  $j$  ( $L_j$ ). The real space moiré of moiré supercell  $A_{mn}^H$  is obtained by  $A_{mn}^H = (1/2\pi)(G_{mn}^H)^{-T}$ , with the norm of its column vectors being the moiré of moiré length. Figure 1(b) shows the dominant moiré of moiré length as a function of twist angles in which each lobe corresponds to

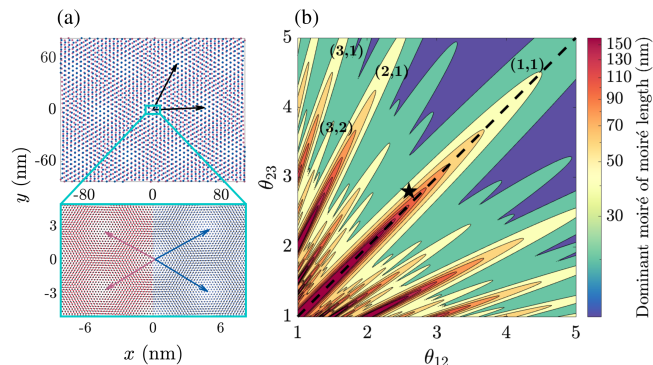


FIG. 1. Illustration of moiré of moiré pattern in tTLG for  $\theta_{12} = 2.6^\circ$ ,  $\theta_{23} = 2.8^\circ$ . (a) Red and blue points represent the lattice points of the bilayer moiré supercells between L1-L2 and L2-L3, respectively. Black arrows represent dominant moiré of moiré supercell lattice vectors. A blowup of the small boxed area is shown below, with points representing monolayer lattice points, for L1 and L2 on the left half and for L2 and L3 on the right half. The moiré lattice vectors (red and blue arrows) are slightly rotated and have different lattice constants. (b) The dominant moiré of moiré length on a logarithmic color scale. The black star corresponds to the twist angle in (a), and  $(m, n)$  labels the dominant moiré of moiré harmonic in the nearby lobe. Black dashed line represents  $\theta_{12} = \theta_{23}$ .

the region where a different harmonic  $(m, n)$  dominates. The moiré of moiré patterns can be discerned visually only near the  $(N, 1)$  or  $(1, N)$  lobes for  $N \in \mathbb{Z}$ . Generally, multiple harmonics have competing length scales (see Supplemental Material [22], Sec. I). Therefore, tTLG cannot be approximated by two aligned tBLG and a general expression for the trilayer supercell does not exist, making it fundamentally different than multilayered vdW heterostructures with a single twist angle [25–28]. The lack of a supercell approximation and the large length scale pose many computational challenges to the theoretical modeling of tTLG. While there have been some theoretical studies of tTLG [19,29,30], including an accurate treatment of any twist angles by Amorim and Castro [29], an electronic structure model incorporating both accuracy and efficiency is lacking; this severely restricts our ability to investigate its electronic properties and the potential for correlated phases, which have been observed recently in tTLG at the moiré of moiré scale [31].

Here, we present tTLG as a platform to precisely tune twistrionic correlations, using the VHS intensity as a proxy for strong correlations. We derive a general momentum-space model to study the electronic properties of the two-independent-twist-angle tTLG system using a low-energy  $k \cdot p$  model that provides computational efficiency and removes the constraint on the twist angle in atomistic calculations with supercells. Using this model, we explore the tTLG phase space. We find that the two bilayer moiré superlattices hybridize when the two twist angles are equal, minimizing the separation between the two lowest VHS at a critical angle. At general twist angles, there exists a wide range of values at which the VHS merge and the DOS is sharply peaked at the charge-neutrality point (CNP). These magic angles can be understood as a tBLG magic angle modified by an incommensurate perturbative potential from the third layer. Our analysis is well suited to guide experimental searches for correlation effects and enables the interpretation of otherwise unclear experimental findings [31].

*Momentum-space Hamiltonian.*—To obtain the electronic structure model for tTLG, we employ a momentum-space method by taking the Fourier transform of the real-space tight-binding model. At a momentum  $\mathbf{k}$  (referred to as the center site), the model can be formally represented by a  $3 \times 3$  block matrix:

$$\mathcal{H}(\mathbf{k}) = \begin{bmatrix} H^1(\mathbf{k}) & T^{12} & 0 \\ T^{12\dagger} & H^2(\mathbf{k}) & T^{23} \\ 0 & T^{23\dagger} & H^3(\mathbf{k}) \end{bmatrix}. \quad (1)$$

The diagonal blocks are the monolayer graphene tight-binding Hamiltonians in the rotated basis [32] representing the intralayer hopping. The off-diagonal blocks represent the interlayer hopping. The interlayer terms that connect two momentum degrees of freedom  $\mathbf{k}^{(i)}$  and  $\mathbf{k}^{(j)}$  in  $L_i$  and  $L_j$  are given as

$$T_{\alpha\beta}^{ij}[\mathbf{k}^{(i)}, \mathbf{k}^{(j)}] = \frac{1}{|\Gamma|} \sum_{\mathbf{G}^{(i)}, \mathbf{G}^{(j)}} e^{i\mathbf{G}^{(i)} \cdot \tau_\alpha^{(i)}} \tilde{t}_{\alpha\beta}^{ij}[\mathbf{k} + \mathbf{k}^{(i)} + \mathbf{G}^{(i)}] e^{-i\mathbf{G}^{(j)} \cdot \tau_\beta^{(i)}} \times \delta_{\mathbf{k}^{(i)} - \mathbf{G}^{(i)}, \mathbf{k}^{(j)} - \mathbf{G}^{(j)}}, \quad (2)$$

where  $|\Gamma|$  is the monolayer unit cell area,  $\tau_\alpha$  ( $\tau_\beta$ ) is the position of the sublattice  $\alpha$  ( $\beta$ ),  $\mathbf{G}^{(\ell)}$  is a reciprocal space lattice vector in  $L_\ell$ , and  $\tilde{t}_{\alpha\beta}^{ij}(\mathbf{p})$  is the momentum-space hopping parameter between sublattice  $\alpha$  in  $L_i$  and sublattice  $\beta$  in  $L_j$ . The  $\delta$  function imposes the constraint on the values of  $\mathbf{k}^{(\ell)}$ , dictating the interlayer scattering selection rule. The above expressions are equivalent to a real-space tight-binding model in the Bloch basis (see Supplemental Material [22], Sec. II A, for derivation).

Unlike tBLG [33–37], the momentum-space basis in tTLG is infinitely dimensional and lacks a Brillouin zone even in the continuum limit. In bilayers, coupled momentum states satisfy the selection rule  $\mathbf{k}^{(1)} - \mathbf{k}^{(2)} = \mathbf{G}^{(1)} - \mathbf{G}^{(2)}$  [35]. Note that for a given  $\mathbf{G}^{(1)} = m\mathbf{b}_1^{(1)} + n\mathbf{b}_2^{(1)}$  for  $m, n \in \mathbb{Z}$ , we also have  $\mathbf{G}^{(2)} = m\mathbf{b}_1^{(2)} + n\mathbf{b}_2^{(2)}$  for the same  $m, n$ , where  $\mathbf{b}_i^{(\ell)}$  is the  $i$ th component of the primitive reciprocal lattice vector of  $L_\ell$ , since other hopping processes are much higher in energy. As  $|\mathbf{G}^{(\ell)}|$  increases, the scattered momentum  $\mathbf{k}'$  becomes farther away from the Dirac point. Therefore, to implement a finite cutoff, we can simply constrain the magnitude of the scattered momentum  $\mathbf{k}' = \mathbf{G}^{(\ell)}$  for  $\ell = 1, 2$ . Physically,  $\mathbf{k}'$  is a monolayer reciprocal lattice vector that can scatter to a nearby momentum in the other layer. In contrast, in trilayers, the momentum states that form the basis of the Hamiltonian are connected in a more complicated way. A given  $\mathbf{k}^{(1)}$  can couple to a momentum state  $\mathbf{k}^{(2)}$  that satisfies  $\mathbf{k}^{(2)} = \mathbf{k}^{(1)} + \mathbf{G}^{(2)} - \mathbf{G}^{(1)}$ , same as in bilayers. Each  $\mathbf{k}^{(2)}$  can then couple to a momentum state  $\mathbf{k}^{(3)}$  through the second selection rule [Eq. (2)], resulting in the following final momentum:

$$\mathbf{k}^{(3)} = \mathbf{k}^{(1)} + [\mathbf{G}^{(2)} - \mathbf{G}^{(1)}] + [\mathbf{G}^{(3)} - \mathbf{G}'^{(2)}], \quad (3)$$

where the reciprocal lattice vectors satisfy  $\mathbf{G}^{(2)} - \mathbf{G}^{(1)} = m\mathbf{b}_1^{(12)} + n\mathbf{b}_2^{(12)}$  and  $\mathbf{G}^{(3)} - \mathbf{G}'^{(2)} = m'\mathbf{b}_1^{(23)} + n'\mathbf{b}_2^{(23)}$  for  $m, n, n', m' \in \mathbb{Z}$ , with  $\mathbf{b}_k^{(ij)} = \mathbf{b}_k^{(j)} - \mathbf{b}_k^{(i)}$  being the bilayer moiré reciprocal space lattice vectors. Equation (3) suggests that L1 and L3 are coupled through L2, even though a direct interlayer hopping is not allowed. Unlike the simple 2D momentum crystal in bilayers, here the incommensuration between  $\mathbf{b}_k^{(12)}$  and  $\mathbf{b}_k^{(23)}$  creates for  $\mathbf{k}^{(3)}$  a 4D structure that is projected onto 2D.

Equation (3) suggests that in  $L_\ell$  of tTLG,  $\mathbf{k}'$  is given by  $\mathbf{k}' = \mathbf{G}^{(i)} + \mathbf{G}^{(j)}$  for  $\ell \neq i, j$ . To implement a cutoff, we should impose  $|\mathbf{k}'| \leq k_c$  for some cutoff value  $k_c$ . However, the incommensurability of twisted trilayers suggests that  $|\mathbf{k}'|$  can be arbitrarily small and imposing  $|\mathbf{k}'| \leq k_c$  still

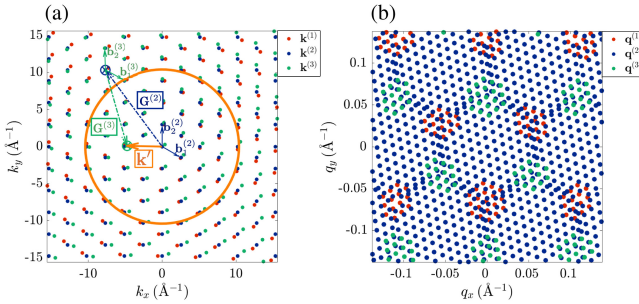


FIG. 2. Momentum degrees of freedom for tTLG at  $\theta_{12} = 2.2^\circ$ ,  $\theta_{23} = 2^\circ$ . Red, blue, and green are the reciprocal lattice vectors of L1, L2, and L3, respectively. The origin is the Dirac point of L2. (a) Extended zone scheme, with the orange circle indicating the cutoff in  $|\mathbf{k}'|$ .  $\mathbf{k}' = \mathbf{G}^{(2)} + \mathbf{G}^{(3)}$  falls within the cutoff radius  $10 \text{\AA}^{-1}$  despite both  $|\mathbf{G}^{(2)}|$  and  $|\mathbf{G}^{(3)}|$  being large. The momenta of L3 are centered at  $\mathbf{G}^{(2)}$ . (b) Reduced zone scheme folded back to the monolayer Dirac points,  $\mathbf{q}^{(\ell)} = \mathbf{k}^{(\ell)} - K_{L\ell}$ . This basis corresponds to the same twist angle as (a) but with an additional constraint  $|\mathbf{G}^{(\ell)}| \leq k_c = 6|\mathbf{b}^{(\ell)}|$ , leading to 26 921 momenta.

leads to an infinite basis. For example, in Fig. 2(a), even though  $\mathbf{G}^{(2)}$  lies outside of the cutoff, the resulting  $\mathbf{k}'$  is still a relevant low-energy degree of freedom due to the two-step scattering process. A similar construction can be made for all other  $\mathbf{G}^{(2)}$  outside of the cutoff radius, which means within a finite cutoff, there are infinitely many coupled momentum states. In practice, another set of cutoff conditions needs to be implemented, namely  $|\mathbf{G}^{(\ell)}| \leq k_c$ . With the constraint on  $|\mathbf{G}^{(\ell)}|$ , the  $\mathbf{k}'$  in Fig. 2(a) is no longer allowed. In this way, we ignore the cases where  $|\mathbf{G}^{(\ell)}|$  is large but  $|\mathbf{k}'|$  is small, leading to the neglect of some low-energy degrees of freedom and hence convergence is not guaranteed, which merits future work (see Supplemental Material [22], Sec. IID, for convergence study). In this work, we choose  $k_c = 4|\mathbf{b}^{(\ell)}|$ , with  $\sim 5600$  momenta, such that the properties of interest (e.g., DOS maximum and the VHS location) do not change significantly as  $k_c$  increases.

We take the low-energy limit by expanding around the Dirac point of each layer,  $K_{L\ell}$ , letting  $\mathbf{k}^{(\ell)} = \mathbf{q}^{(\ell)} + K_{L\ell}$ , which simplifies the model proposed by Amorim and Castro [29]. The intralayer Hamiltonian becomes the rotated Dirac equation,  $H^\ell = v_F \mathbf{q} \cdot (\sigma_x^{\theta_\ell}, -\sigma_y^{\theta_\ell})$ , where  $\sigma_x^{\theta_\ell} = \sigma_x \cos \theta_\ell - \sigma_y \sin \theta_\ell$  and  $\sigma_y^{\theta_\ell} = \sigma_x \sin \theta_\ell + \sigma_y \cos \theta_\ell$  are rotated Pauli matrices with  $\theta_1 = \theta_{12}, \theta_2 = 0, \theta_3 = -\theta_{23}$ ,  $v_F = 0.8 \times 10^6 \text{ cm/s}$  is the Fermi velocity [38], and  $\mathbf{q} = \mathbf{k} + \mathbf{k}^{(\ell)} - K_{L\ell}$ . For the interlayer hopping, we make the approximation that  $\tilde{t}_{\alpha\beta}^{ij}[\mathbf{k} + \mathbf{k}^{(i)} + \mathbf{G}^{(i)}] \approx \tilde{t}_{\alpha\beta}^{ij}[\mathbf{G}^{(i)} + K_{Li}]$  since  $|\mathbf{k}|, |\mathbf{q}^{(i)}| \ll |K_{Li}|, |\mathbf{G}^{(i)}|$ , for  $\mathbf{k}$  near the Dirac point. Due to the rapid decay of  $\tilde{t}_{\alpha\beta}^{ij}(\mathbf{p})$  as  $\mathbf{p}$  increases [2,38,39], we keep only the first shell in the summation in Eq. (2):

$$T_{\alpha\beta}^{ij}[\mathbf{q}^{(i)}, \mathbf{q}^{(j)}] = \sum_{n=1}^3 T_{n,\alpha\beta}^{ij} \delta_{\mathbf{q}^{(i)} - \mathbf{q}^{(j)}, -\mathbf{q}_n^{ij}}, \quad (4)$$

where  $\mathbf{q}_1^{ij} = K_{Li} - K_{Lj}$ ,  $\mathbf{q}_2^{ij} = \mathcal{R}^{-1}(2\pi/3)\mathbf{q}_1^{ij}$ , and  $\mathbf{q}_3^{ij} = \mathcal{R}(2\pi/3)\mathbf{q}_1^{ij}$  using a counterclockwise rotation matrix  $\mathcal{R}(\theta)$ . We include out-of-plane relaxation by letting  $t_{AA}^{ij} = t_{BB}^{ij} = \omega_0 = 0.07 \text{ eV}$  and  $t_{AB}^{ij} = t_{BA}^{ij} = \omega_1 = 0.11 \text{ eV}$  [34,40]. In the matrix form,

$$T_1^{ij} = \begin{bmatrix} \omega_0 & \omega_1 \\ \omega_1 & \omega_0 \end{bmatrix}, \quad T_2^{ij} = \begin{bmatrix} \omega_0 & \omega_1 \bar{\phi} \\ \omega_1 \phi & \omega_0 \end{bmatrix}, \quad T_3^{ij} = \bar{T}_2^{ij}, \quad (5)$$

where  $\phi = \exp(i2\pi/3)$  and  $\bar{z}$  indicates the complex conjugate of  $z$ . In tBLG, with the low-energy expansion, momenta  $\mathbf{q}^{(1)}$  and  $\mathbf{q}^{(2)}$  form a hexagonal lattice with the neighboring hexagon corners representing states from alternating layers (a moiré momentum lattice) [2,35]. In tTLG, on top of each lattice point of the L1-L2 moiré momentum lattice, the additional scattering process creates a copy of the L2-L3 moiré momentum lattice [Fig. 2(b)], suggesting the absence of a Brillouin zone.

*Density of states.*—We use Gaussian smearing to obtain the total DOS, summing over the two bilayer moiré Brillouin zones, each discretized using a  $22 \times 22$  grid [41] (see Supplemental Material [22], Sec. II C, for the expression). For normalization, we first calculate the DOS of only the intralayer Hamiltonian, which reduces to three independent copies of monolayer graphene [32]. We then obtain the normalization constant by fixing the prefactor to the expected low-energy monolayer DOS and using the same constant for the DOS of the full Hamiltonian. We adapt the Gaussian FWHM  $\kappa$  based on the twist angle  $\theta_{\ell,\ell+1}$ : for  $\theta_{\ell,\ell+1} \leq 2^\circ$ ,  $\kappa = 0.35 \text{ meV}$ ; for  $\theta_{\ell,\ell+1} \in (2^\circ, 3.9^\circ]$ ,  $\kappa = 1.2 \text{ meV}$ ; for  $\theta_{\ell,\ell+1} > 3.9^\circ$ ,  $\kappa = 2.4 \text{ meV}$ .

*Evolution of VHS.*—We explore next the behavior of VHS as a function of twist angles in tTLG by investigating the DOS enhancement and the narrowing of the separation between VHS (referred to as the VHS gap). We define a magic angle approximately as a geometry where both features are achieved. Figure 3(a) shows the DOS of tTLG at  $\theta_{12} = \theta_{23}$ . The bright regions represent VHS. As the twist angle decreases, the VHS gap first decreases and then increases after reaching a minimum at  $\sim 2.1^\circ$ . This behavior is similar to the evolution of VHS in tBLG in which changing the twist angle tunes the hybridization between two monolayer Dirac cones. In tTLG with  $\theta_{12} = \theta_{23}$ , varying the twist angle changes the hybridization strength between the two identical bilayer moiré superlattices. However, the two VHS can never merge at the CNP, with the minimum VHS gap being  $\sim 20 \text{ meV}$  at  $2.1^\circ$ . The DOS is also orders of magnitude lower than at the tBLG magic angle. For general twist angles, Fig. 3(b) shows the DOS as a function of  $\theta_{12}$  with  $\theta_{23} = 3^\circ$ . Unlike when  $\theta_{12} = \theta_{23}$ , the two VHS approach each other as the

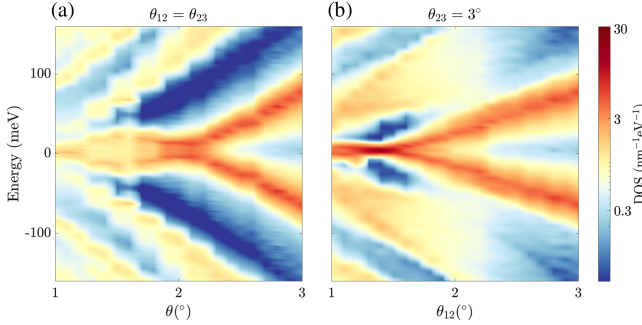


FIG. 3. (a) DOS as a function of twist angle for  $\theta_{12} = \theta_{23}$ , (b) DOS as a function  $\theta_{12}$  at  $\theta_{23} = 3^\circ$ , both on a logarithmic color scale.

twist angle decreases and merge when  $1.3^\circ \leq \theta_{12} \leq 1.6^\circ$ , resulting in a sharp DOS peak.

To investigate the nature of DOS enhancements in tTLG, we performed calculations over an entire region of the  $\theta_{12}$ ,  $\theta_{23}$  parameter space. Figure 4 shows the DOS maximum and the VHS gap,  $\Delta E$ , as a function of both twist angles [42]. The magic-angle condition is met at a wide range of twist angles that follows a smooth curve but disappears near the diagonal. Although there is no significant DOS enhancement at  $\theta_{12} = \theta_{23}$ , the DOS maximum is higher compared to the nearby regions where  $\theta_{12}$  and  $\theta_{23}$  differ slightly [light yellow region within the dotted lines in Fig. 4(a)].

We now examine the magic angles away from the diagonal. In the limit where  $\theta_{12} \gg \theta_{23}$  or  $\theta_{12} \ll \theta_{23}$ , tTLG decomposes into a decoupled tBLG moiré supercell and a graphene monolayer; the monolayer does not contribute significantly to the low-energy features. Therefore, we observe that the tTLG magic-angle curve asymptotically approaches the tBLG magic angle [dashed lines in Fig. 4(a)].

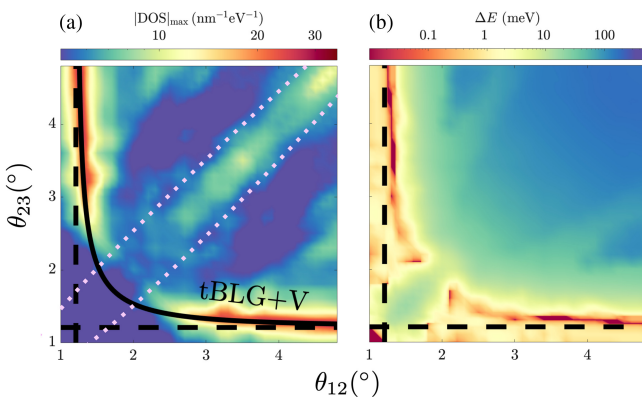


FIG. 4. (a) DOS maximum and (b) VHS gap,  $\Delta E$ , as a function of twist angles on a logarithmic color scale. The black solid line follows the tTLG magic angles predicted by Eq. (7). Vertical and horizontal black dashed lines correspond to  $\theta_{12}$  and  $\theta_{23}$  at the tBLG magic angle, respectively. Within the dotted lines is roughly the region that can be understood as the hybridization between two bilayer moiré superlattices.

for large  $\theta_{12}$  or  $\theta_{23}$ . We verified numerically that when one twist angle is very large,  $\theta_{12} = 40^\circ$  for instance, the DOS maximum occurs exactly when  $\theta_{23}$  is at the tBLG magic angle. The continuous curve and its asymptotic behavior suggest that these magic angles can be understood as the magic-angle tBLG modified by an effective potential,  $V$ , from the third layer. We can qualitatively analyze this argument using perturbation theory by truncating the momentum space to the first shell, including one state from L2 and three states each from L1 and L3. We obtain the renormalized Fermi velocity  $v_F^*$  by extracting the coefficient of the first-order effective Hamiltonian in  $\mathbf{q}$  in the form of a Dirac Hamiltonian, given by

$$v_F^* = \frac{1 - 3(\alpha_{12}^2 + \alpha_{23}^2)}{1 + 6(\alpha_{12}^2 + \alpha_{23}^2)} v_F, \quad (6)$$

where  $\alpha_{ij} = \omega/(v_F k_{\theta_{ij}})$ ,  $k_{\theta_{ij}} = 8\pi \sin(\theta_{ij}/2)/(3a_G)$ , assuming that  $\omega_0 = \omega_1 = \omega$ . The Hamiltonian and its derivation are provided in Sec. III of the Supplemental Material [22]. Magic angles occur when  $v_F^*$  vanishes, leading to the following condition:

$$\alpha_{12}^2 + \alpha_{23}^2 = \frac{1}{3}. \quad (7)$$

The solid line in Fig. 4(a) corresponds to  $\theta_{12}$  and  $\theta_{23}$  that satisfy Eq. (7), which matches the DOS peaks and  $\Delta E$  minima in Fig. 4(a),(b). Taking the large angle limit, for example, when  $\theta_{23} \rightarrow \infty$ ,  $\alpha_{23} \rightarrow 0$ , Eq. (7) becomes  $\alpha_{12}^2 = \frac{1}{3}$ , which is the tBLG magic-angle condition [2].

The evolution of VHS along the diagonal likely has a different origin than the magic angles for  $\theta_{12} \neq \theta_{23}$ . Perturbation theory predicts that  $v_F^*$  can reach 0 at  $\theta_{12} = \theta_{23} = 1.72^\circ$ . In the numerical calculations, however, we do not observe  $v_F^* = 0$  at equal twist angles, and the twist angle with the minimal VHS gap ( $2.1^\circ$ ) deviates from the perturbation theory prediction. The discrepancy suggests that the perturbation argument does not apply to equal twist angles since features near the diagonal are more aptly described by the hybridization between the two bilayer moiré superlattices with a shared middle layer rather than between two independent unit cells as in tBLG.

*Moiré of moiré.*—In magic-angle tBLG, correlated states occur at the half-filling of the moiré supercell by filling two isolated flatbands [3,4,16–18]. In tTLG, even though the origin of some magic angles is perturbed tBLG, filling each flatband corresponds to filling the moiré of moiré supercell rather than the bilayer moiré cell because the incommensurate effective potential modifies the relevant supercell area.

We compare our results to a simplified model that approximates tTLG as two aligned moiré cells [30]. While we observe similar qualitative behaviors, the simplified model fails to capture physics at the moiré of moiré scale and does not predict as drastic a DOS enhancement as

our work. Moreover, the simplified model requires a new basis for different sets of twist angles, making it difficult to generalize—limitations that our model overcomes. We include a comparison between the two models in Sec. IV of the Supplemental Material [22].

In summary, we explore the rich electronic behavior of tTLL in its twist-angle phase space. We offer a general low-energy momentum-space model to obtain electronic structure in tTLL. We show that the twisted trilayer momentum-space model does not have a Brillouin zone and has an infinitely sized basis. Although we do not predict correlation strengths directly, we can use the presence of VHS as a proxy for electronic correlation. We show that the tTLL system exhibits a wide range of magic angles with merging VHS at the CNP. Away from equal twist angles, the origin of the magic angles can be understood as tBLG in an incommensurate perturbative potential. At equal twist angles, the electronic properties are a result of the hybridization between two bilayer moiré superlattices that share the middle layer. Tuning the twist angle makes it possible to traverse between these two regimes. Our MATLAB code for the model is openly available [43].

We thank Ke Wang, Xi Zhang, Kan-Ting Tsai, Francisco Guinea, Philip Kim, and Paul Cazeaux for helpful discussions. This work was supported by the STC Center for Integrated Quantum Materials, NSF Grant No. DMR-1231319, ARO MURI Grant No. W911NF-14-0247, and NSF DMREF Grant No. 1922165. Calculations were performed on the Odyssey cluster supported by the FAS Division of Science, Research Computing Group at Harvard University.

- 
- [1] S. Carr, D. Massatt, S. Fang, P. Cazeaux, M. Luskin, and E. Kaxiras, Twistrionics: Manipulating the electronic properties of two-dimensional layered structures through their twist angle, *Phys. Rev. B* **95**, 075420 (2017).
- [2] R. Bistritzer and A. H. MacDonald, Moiré bands in twisted double-layer graphene, *Proc. Natl. Acad. Sci. U.S.A.* **108**, 12233 (2011).
- [3] Y. Cao, V. Fatemi, A. Demir, S. Fang, S. L. Tomarken, J. Y. Luo, J. D. Sanchez-Yamagishi, K. Watanabe, T. Taniguchi, E. Kaxiras, R. C. Ashoori, and P. Jarillo-Herrero, Correlated insulator behaviour at half-filling in magic-angle graphene superlattices, *Nature (London)* **556**, 80 (2018).
- [4] Y. Cao, V. Fatemi, S. Fang, K. Watanabe, T. Taniguchi, E. Kaxiras, and P. Jarillo-Herrero, Unconventional superconductivity in magic-angle graphene superlattices, *Nature (London)* **556**, 43 (2018).
- [5] G. Chen, L. Jiang, S. Wu, B. Lyu, H. Li, B. L. Chittari, K. Watanabe, T. Taniguchi, Z. Shi, J. Jung, Y. Zhang, and F. Wang, Evidence of a gate-tunable Mott insulator in a trilayer graphene moiré superlattice, *Nat. Phys.* **15**, 237 (2019).
- [6] M. Yankowitz, J. Jung, E. Laksono, N. Leconte, B. L. Chittari, K. Watanabe, T. Taniguchi, S. Adam, D. Graf, and C. R. Dean, Dynamic band-structure tuning of graphene moiré superlattices with pressure, *Nature (London)* **557**, 404 (2018).
- [7] M. Yankowitz, S. Chen, H. Polshyn, Y. Zhang, K. Watanabe, T. Taniguchi, D. Graf, A. F. Young, and C. R. Dean, Tuning superconductivity in twisted bilayer graphene, *Science* **363**, 1059 (2019).
- [8] C. Shen, N. Li, S. Wang, Y. Zhao, J. Tang, J. Liu, J. Tian, Y. Chu, K. Watanabe, T. Taniguchi, R. Yang, Z. Y. Meng, D. Shi, and G. Zhang, Correlated states in twisted double bilayer graphene, *Nat. Phys.* **16**, 520 (2020).
- [9] X. Liu, Z. Hao, E. Khalaf, J. Y. Lee, Y. Ronen, H. Yoo, D. H. Najafabadi, K. Watanabe, T. Taniguchi, A. Vishwanath *et al.*, Tunable spin-polarized correlated states in twisted double bilayer graphene, *Nature (London)* **583**, 221 (2020).
- [10] Y. Cao, D. Rodan-Legrain, O. Rubies-Bigorda, J. M. Park, K. Watanabe, T. Taniguchi, and P. Jarillo-Herrero, Electric field tunable correlated states and magnetic phase transitions in twisted bilayer-bilayer graphene, *Nature (London)* **583**, 215 (2020).
- [11] G. W. Burg, J. Zhu, T. Taniguchi, K. Watanabe, A. H. MacDonald, and E. Tutuc, Correlated Insulating States in Twisted Double Bilayer Graphene, *Phys. Rev. Lett.* **123**, 197702 (2019).
- [12] L. Wang, E.-M. Shih, A. Ghiootto, L. Xian, D. A. Rhodes, C. Tan, M. Claassen, D. M. Kennes, Y. Bai, B. Kim, K. Watanabe, T. Taniguchi, X. Zhu, J. Hone, A. Rubio, A. Pasupathy, and C. R. Dean, Magic continuum in twisted bilayer WSe<sub>2</sub>, [arXiv:1910.12147](https://arxiv.org/abs/1910.12147).
- [13] Yu. Saito, J. Ge, K. Watanabe, T. Taniguchi, and A. F. Young, Decoupling superconductivity and correlated insulators in twisted bilayer graphene, [arXiv:1911.13302](https://arxiv.org/abs/1911.13302) [Nat. Phys. (to be published)].
- [14] Z. Zhang, R. Myers, K. Watanabe, T. Taniguchi, and B. J. LeRoy, Probing the Wavefunctions of Correlated States in Magic Angle Graphene, [arXiv:2003.09482](https://arxiv.org/abs/2003.09482) [Phys. Rev. Lett. (to be published)].
- [15] X. Liu, Z. Wang, K. Watanabe, T. Taniguchi, O. Vafek, and J. I. A. Li, Tuning electron correlation in magic-angle twisted bilayer graphene using Coulomb screening, [arXiv:2003.11072](https://arxiv.org/abs/2003.11072).
- [16] M. Koshino, N. F. Q. Yuan, T. Koretsune, M. Ochi, K. Kuroki, and L. Fu, Maximally Localized Wannier Orbitals and the Extended Hubbard Model for Twisted Bilayer Graphene, *Phys. Rev. X* **8**, 031087 (2018).
- [17] H. C. Po, L. Zou, T. Senthil, and A. Vishwanath, Faithful tight-binding models and fragile topology of magic-angle bilayer graphene, *Phys. Rev. B* **99**, 195455 (2019).
- [18] S. Carr, S. Fang, H. C. Po, A. Vishwanath, and E. Kaxiras, Derivation of Wannier orbitals and minimal-basis tight-binding Hamiltonians for twisted bilayer graphene: First-principles approach, *Phys. Rev. Research* **1**, 033072 (2019).
- [19] Z. Zhu, P. Cazeaux, M. Luskin, and E. Kaxiras, Modeling mechanical relaxation in incommensurate trilayer van der waals heterostructures, *Phys. Rev. B* **101**, 224107 (2020).
- [20] M. Andelković, S. P. Milovanović, L. Covaci, and F. M. Peeters, Double moiré with a twist: Super-moiré in encapsulated graphene, *Nano Lett.* **20**, 979 (2020).
- [21] N. Leconte and J. Jung, Commensurate and incommensurate double moiré interference in graphene encapsulated by hexagonal boron nitride, *2D Mater.* **7**, 031005 (2020).

- [22] See Supplementary Material, which includes Refs. [23,24], at <http://link.aps.org/supplemental/10.1103/PhysRevLett.125.116404> for the calculation of moiré of moiré length, a detailed derivation of the momentum-space model and convergence test, the derivation of the analytical expression of the tTlG magic angles, and comparisons with other models.
- [23] M. Yankowitz, J. Xue, D. Cormode, J. D. Sanchez-Yamagishi, K. Watanabe, T. Taniguchi, P. Jarillo-Herrero, P. Jacquod, and B. J. Leroy, Emergence of superlattice Dirac points in graphene on hexagonal boron nitride, *Nat. Phys.* **8**, 382 (2012).
- [24] W.-J. Zuo, J.-B. Qiao, D.-L. Ma, L.-J. Yin, G. Sun, J.-Y. Zhang, L.-Y. Guan, and L. He, Scanning tunneling microscopy and spectroscopy of twisted trilayer graphene, *Phys. Rev. B* **97**, 035440 (2018).
- [25] X. Li, F. Wu, and A. H. MacDonald, Electronic structure of single-twist trilayer graphene, [arXiv:1907.12338](https://arxiv.org/abs/1907.12338).
- [26] S. Carr, C. Li, Ziyuan Zhu, E. Kaxiras, S. Sachdev, and A. Kruchkov, Ultraheavy and ultrarelativistic dirac quasi particles in sandwiched graphenes, *Nano Lett.* **20**, 3030 (2020).
- [27] S. Chen, M. He, Y.-H. Zhang, V. Hsieh, Z. Fei, K. Watanabe, T. Taniguchi, D. H. Cobden, X. Xu, C. R. Dean, and M. Yankowitz, Electrically tunable correlated and topological states in twisted monolayer-bilayer graphene, [arXiv:2004.11340](https://arxiv.org/abs/2004.11340).
- [28] Y. Park, B. L. Chittari, and J. Jung, Gate-tunable topological flat bands in twisted monolayer-bilayer graphene, *Phys. Rev. B* **102**, 035411 (2020).
- [29] B. Amorim and E. V. Castro, Electronic spectral properties of incommensurate twisted trilayer graphene, [arXiv:1807.11909](https://arxiv.org/abs/1807.11909).
- [30] C. Mora, N. Regnault, and B. A. Bernevig, Flatbands and Perfect Metal in Trilayer Moiré Graphene, *Phys. Rev. Lett.* **123**, 026402 (2019).
- [31] K.-T. Tsai, X. Zhang, Z. Zhu, Y. Luo, S. Carr, M. Luskin, E. Kaxiras, and K. Wang, Correlated superconducting and insulating states in twisted trilayer graphene moiré of moiré superlattices, [arXiv:1912.03375](https://arxiv.org/abs/1912.03375).
- [32] A. H. Castro Neto, F. Guinea, N. M. R. Peres, K. S. Novoselov, and A. K. Geim, The electronic properties of graphene, *Rev. Mod. Phys.* **81**, 109 (2009).
- [33] N. N. T. Nam and M. Koshino, Lattice relaxation and energy band modulation in twisted bilayer graphene, *Phys. Rev. B* **96**, 075311 (2017).
- [34] S. Carr, S. Fang, Z. Zhu, and E. Kaxiras, Exact continuum model for low-energy electronic states of twisted bilayer graphene, *Phys. Rev. Research* **1**, 013001 (2019).
- [35] S. Fang, S. Carr, Z. Zhu, D. Massatt, and E. Kaxiras, Angle-dependent *Ab initio* low-energy Hamiltonians for a relaxed twisted bilayer graphene heterostructure, [arXiv:1908.00058](https://arxiv.org/abs/1908.00058).
- [36] F. Guinea and N. R. Walet, Continuum models for twisted bilayer graphene: Effect of lattice deformation and hopping parameters, *Phys. Rev. B* **99**, 205134 (2019).
- [37] N. Leconte, S. Javvaji, J. An, and J. Jung, Relaxation effects in twisted bilayer graphene: A multi-scale approach, [arXiv:1910.12805](https://arxiv.org/abs/1910.12805).
- [38] S. Fang and E. Kaxiras, Electronic structure theory of weakly interacting bilayers, *Phys. Rev. B* **93**, 235153 (2016).
- [39] G. Catarina, B. Amorim, E. V Castro, J. M. V. P. Lopes, and N. Peres, Twisted bilayer graphene: Low-energy physics, electronic and optical properties, in *Handbook of Graphene, Graphene-Like 2D Materials* Vol. 3 (John Wiley & Sons, Ltd., New Jersey, 2019), p. 177.
- [40] N. N. T. Nam and M. Koshino, Lattice relaxation and energy band modulation in twisted bilayer graphene, *Phys. Rev. B* **96**, 075311 (2017).
- [41] D. Massatt, S. Carr, M. Luskin, and C. Ortner, Incommensurate heterostructures in momentum space, *Multiscale Model. Simul.* **16**, 429 (2018).
- [42] The data set consists of a  $43 \times 43$  sampling. A Gaussian convolution kernel is applied for smoothening.
- [43] Z. Zhu, C. Stephen, M. Daniel, L. Mitchell, and K. Efthimios, Model for twisted trilayer graphene: A precisely tunable platform for correlated electrons, <https://github.com/ziyanzzhu/ttlg> (2020).